CrossMark

The Recent LMC–SMC Collision: Timing and Impact Parameter Constraints from Comparison of Gaia LMC Disk Kinematics and N-body Simulations

Yumi Choi[1] , Knut A. G. Olsen[2] , Gurtina Besla[3] , Roeland P. van der Marel[1,4] , Paul Zivick[5] , Nitya Kallivayalil[6] , and David L. Nidever[7]

[1] Space Telescope Science Institute, 3700 San Martin Drive, Baltimore, MD 21218, USA; ychoi@stsci.edu
[2] National Optical-Infrared Astronomy Research Laboratory (NOIRLab), 950 North Cherry Avenue, Tucson, AZ 85719, USA
[3] Department of Astronomy, University of Arizona, 933 North Cherry Avenue, Tucson, AZ 85721, USA
[4] Center for Astrophysical Sciences, Department of Physics & Astronomy, Johns Hopkins University, Baltimore, MD 21218, USA
[5] Mitchell Institute for Fundamental Physics and Astronomy and Department of Physics and Astronomy, Texas A&M University, College Station, TX 77843, USA
[6] Department of Astronomy, University of Virginia, 530 McCormick Road, Charlottesville, VA 22904, USA
[7] Department of Physics, Montana State University, P.O. Box 173840, Bozeman, MT 59717, USA

Abstract

We present analysis of the proper-motion (PM) field of the red clump stars in the Large Magellanic Cloud (LMC) disk using the Gaia Early Data Release 3 catalog. Using a kinematic model based on old stars with 3D velocity measurements, we construct the residual PM field by subtracting the center-of-mass motion and internal rotation motion components. The residual PM field reveals asymmetric patterns, including larger residual PMs in the southern disk. Comparisons of the observed residual PM field with those of five numerical simulations of an LMC analog that is subject to the tidal fields of the Milky Way and the Small Magellanic Cloud (SMC) show that the present-day LMC is not in dynamical equilibrium. We find that both the observed level of disk heating (PM residual rms of 0.057 ± 0.002 mas yr^{-1}) and kinematic asymmetry are not reproduced by Milky Way tides or if the SMC impact parameter is larger than the size of the LMC disk. This measured level of disk heating provides a novel and important method to validate numerical simulations of the LMC–SMC interaction history. Our results alone put constraints on an impact parameter $\lesssim 10$ kpc and impact timing < 250 Myr. When adopting the impact timing constraint of ~ 140–160 Myr ago from previous studies, our results suggest that the most recent SMC encounter must have occurred with an impact parameter of ~ 5 kpc. We also find consistent radial trends in the kinematically and geometrically derived disk inclination and line-of-node position angles, indicating a common origin.

1. Introduction

The Large Magellanic Cloud (LMC) is likely on its first infall toward the Milky Way (e.g., Kallivayalil et al. 2006; Besla et al. 2007; van der Marel & Sahlmann 2016), and thus the Milky Way is not likely the main driver shaping the present-day morphology and kinematics of the LMC main body. Consequently, many studies attribute the origin of the asymmetric appearance of the LMC to the close interactions with its nearby companion, the Small Magellanic Cloud (SMC; e.g., van der Marel & Cioni 2001; Olsen & Salyk 2002; Yoshizawa & Noguchi 2003; Besla et al. 2012, 2013; Yozin & Bekki 2014; Besla et al. 2016; Pardy et al. 2016; Choi et al. 2018a, 2018b). In fact, recent studies of the motion of stars and gas in the Magellanic Bridge and the outskirts of the SMC collectively suggest a direct collision between the LMC and SMC ∼100–250 Myr ago (e.g., Oey et al. 2018; Zivick et al. 2018; Murray et al. 2019; Zivick et al. 2019; Schmidt et al. 2020). The collision is "direct" in that the impact parameter of the encounter is expected to be less than the radius of the LMC's stellar disk (Zivick et al. 2018). Thus, constraining the timing and impact parameter of the LMC–SMC collision is the key to constraining the recent dynamical evolution and current morphology of the Magellanic Clouds (MCs).

Although there have been significant efforts to understand the LMC's internal stellar kinematics, both the lack of a large star sample with accurate and precise 6D phase-space information and the lack of baseline dynamical models to compare against the observations have prevented us from developing a complete picture about the LMC's dynamical evolution.

The advent of large, deep, and MC-targeted photometric surveys over the past decade, e.g., VMC (Cioni et al. 2011), OGLE-IV (Udalski et al. 2015), and SMASH (Nidever et al. 2017), has led to an explosion of new discoveries about the MC's star formation histories, dust distribution, and stellar structure, in both the main bodies and the peripheries. The LMC stellar disk is now known to be warped and twisted, such that the inclination and line-of-node position angles vary with galactic radius (e.g., van der Marel & Cioni 2001; Subramanian & Subramaniam 2013; Choi et al. 2018a). Radial variations of the inclination and line-of-node position angles seem to correlate with two significant warps, one at ∼2.5 kpc (Olsen & Salyk 2002) and the other at ∼5.5 kpc (Choi et al. 2018a), and a tilted off-centered bar (e.g., Zhao & Evans 2000; Zaritsky 2004; Subramaniam & Subramanian 2009a; Choi et al. 2018a).

Many of these and other studies used red clump (RC) stars, which are in the core He-burning stage and have intermediate ages, as tracers (e.g., Girardi & Salaris 2001; Olsen &
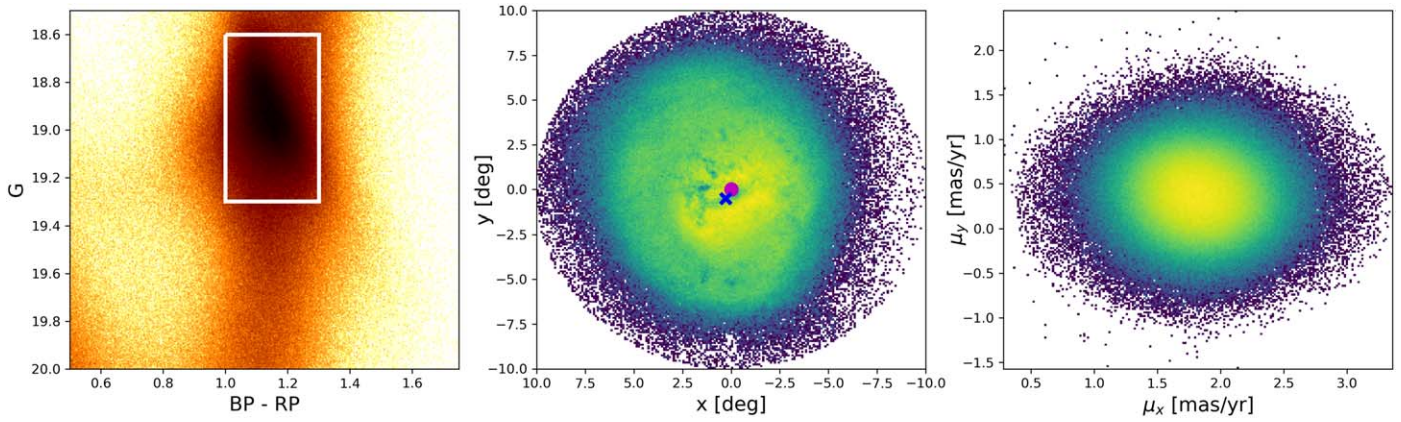
Figure 1. Distributions of the selected RC stars in the Gaia CMD (left), on the sky (middle), and on the PM space (right). The white square in the left panel denotes our CMD selection box. The magenta circle in the middle panel indicates the kinematic center of $(\alpha_0, \delta_0) = (80°443, -69°272)$ derived from the observed stellar kinematics in this study (see Section 3), while the blue cross indicates the photometric center of $(\alpha_0, \delta_0) = (81°275, -69°783)$ by van der Marel (2001).

Salyk 2002; Subramanian & Subramaniam 2009b; Haschke et al. 2011; Girardi 2016; Choi et al. 2018a, 2018b; Górski et al. 2020; Skowron et al. 2021, references therein). RC stars are abundant in the LMC out to $\sim 10°$ from its center and trace well the spatial distribution of underlying older stellar populations (e.g., Choi et al. 2018b). Their uniform stellar core mass at He ignition makes them have very similar effective temperatures and luminosities, which translates to narrow ranges of color and magnitude, respectively.

In this paper, we utilize RC stars with proper-motion (PM) measurements from the early third data release of Gaia (Gaia Collaboration et al. 2021a) in order to study their kinematics in the context of the geometrical knowledge already constrained from these stellar populations. To assist our analysis, we rely on a model fit to a sample consisting mainly of red giant branch (RGB) and asymptotic giant branch (AGB) stars, for which we have observed 3D velocities but no distances as for the RC stars. We compare the RC PMs against these empirically constrained kinematic models and use hydrodynamic N-body simulations by Besla et al. (2012) to assess the dynamical state of the present-day LMC disk and determine whether the data are consistent with theoretical expectations for the disk after a recent encounter with the SMC.

This paper is organized as follows. In Section 2, we describe the Gaia data for the RC sample used in this study. In Section 3, we describe our sample with 3D velocity measurements and kinematic fitting process. We then present the best-fit kinematic model based on the stars that have 3D velocity information. In Section 4, we present the internal and residual PM fields of the RC stars in the LMC. We also compare the radial trend of the geometrically and kinematically measured disk inclination and line-of-node position angles to explore the potential connection between stellar geometry and kinematics. In Section 5, we describe the numerical simulations used in this study and make a detailed comparison of them with the observed LMC to constrain the recent collision between the LMC and SMC. Section 6 summarizes our findings and conclusions.

2. Gaia-selected Red Clump Stars in the LMC

We select the LMC RC stars from the Gaia EDR3 catalog using the following criteria:

1. $50° \leqslant \alpha \leqslant 110°$ and $-80° \leqslant \delta \leqslant -55°$
2. $\varpi < 0.1$ and $\varpi/\sigma_\varpi < 5$ (Gaia Collaboration et al. 2021b)

3. $(\mu_{\alpha*}{-}1.8593)^2 + (\mu_\delta{-}0.3747)^2 < 1.5^2$
4. `astrometric_excess_noise` < 0.2
5. $1.0 \leqslant$ `phot_bp_mean_mag` $-$ `phot_rp_mean_mag` $\leqslant 1.3$
6. $18.6 \leqslant$ `phot_g_mean_mag` $\leqslant 19.3$
7. $|C^*| < 3\sigma_{C^*}$ (Riello et al. 2021)
8. $\rho < 10°$,

where ϖ is parallax in mas; $\mu_{\alpha*}$ and μ_δ are PMs in R.A. (R.A.; α, $\alpha^* = \alpha \cos \delta$) and decl. (decl.; δ) in mas yr^{-1}, respectively; $|C^*|$ is the corrected BP and RP flux excess; and ρ is galactic radius from the LMC kinematic center. Our stringent selection criteria successfully exclude stars with renormalized unit weight error (`ruwe`) > 1.17 and `astrometric_excess_noise_sig` > 0.29, assuring that our final catalog consists of single stars with good astrometric solutions (`ruwe` < 1.4, `astrometric_excess_noise_sig` < 2; Lindegren et al. 2021) and consistent photometry between the G-band magnitude and BP$-$RP color (Riello et al. 2021).

Figure 1 shows the distributions of the selected RC stars in the Gaia color$-$magnitude diagram (CMD), on the sky, and in the PM space. The above criteria secure a clean LMC RC sample, resulting in a total of 975,637 stars. We do not include significantly reddened RC stars, which are redder and fainter, to keep only brighter RC stars with smaller errors in the PM measurements. The possible contamination of RGB stars ($\sim 10\%$ level; Choi et al. 2018a) does not impact the present study, as we do not expect them to be kinematically distinct from the RC stars. In fact, Gaia Collaboration et al. (2021b) revealed almost identical rotation and radial velocity curves for the RC and RGB populations. Following Gaia Collaboration et al. (2021b), we perform our analysis on the (x, y) orthographic projection plane (see their Equations (1)–(3)).

Even with the significantly improved completeness of Gaia (Gaia Collaboration et al. 2021a, 2021b), the RC star census is incomplete along the bar owing to crowding; the fainter, the less complete. However, this incomplete nature of a sample does not matter for stellar kinematic studies because stars in a given population (e.g., RC stars) of different brightness should have statistically identical kinematics particularly when one does not suffer from the small number statistics, which is our case. In other words, for a given stellar population, the overall kinematic properties measured in a subregion with lower completeness should be the same as those in the same

subregion that would be measured if completeness were 100%. We, in fact, explore the kinematics of RC stars brighter and fainter than $G = 18.9$ (Boubert & Everall 2020) and conclude that our results do not depend on the selected brightness of the RC sample.

3. Kinematic Model

To investigate the internal kinematics of the LMC's stellar disk, we fit a model to a sample of ~10,000 stars with PMs from Gaia EDR3 (Gaia Collaboration et al. 2021a) and line-of-sight velocities from the Hydra-CTIO observations of 4226 stars by Olsen et al. (2011), 556 unpublished Hydra-CTIO observations (K. A. G. Olsen et al. 2022, in preparation) processed in an identical way to those in Olsen et al. (2011), and 5386 stars from SDSS DR16/APOGEE-2 (Ahumada et al. 2020). The sample contains predominantly evolved older stars, including RGB and AGB stars, but also ≲1000 red supergiants.

Our modeling procedure, which is based on the formalism of van der Marel et al. (2002), fits up to 12 parameters jointly to the PM and line-of-sight velocity data. The parameters are the location of the kinematic center in R.A. and decl., the bulk transverse motion along the R.A. and decl. axes, the line-of-sight velocity of the kinematic center, the position angle of the line of nodes, the inclination of the disk, two parameters describing the shape and amplitude of the internal rotation curve, and the velocity dispersion in three orthogonal directions. Throughout we assume that the LMC disk has no precession or nutation and that the distance to the LMC is 50.1 kpc (Freedman et al. 2001).

To determine the best-fit parameters, we use a combination of the Python package lmfit (https://lmfit.github.io/lmfit-py/) to find the maximum likelihood parameter values and v3.0.2 of the Markov Chain Monte Carlo package emcee (Foreman-Mackey et al. 2013, 2019) for the final determination of the parameters and their covariances from the posterior probability distributions. We assume uniform priors for all of the parameters, with conservative limits for each based on physical and empirical expectations. The likelihood function is constructed as the product of Gaussian distributions in each of the observed velocity components (line of sight and the two axes of the PM vectors) with respect to the model values. We use 200 walkers and 50,000 steps for the chains, which typically yielded chains 100× to 200× longer than the autocorrelation time. Depending on the convergence of each fit, the first 600–1500 steps are discarded as burn-in.

For this paper, our goal is to derive a model describing the bulk kinematic properties, including internal disk rotation, of our sample of RC stars, the main tracer of this study. Unfortunately, the LMC RC stars are too faint to obtain spectra for line-of-sight velocity measurements. We thus instead use AGB and RGB stars that have both line-of-sight velocities and PMs as surrogates for the RC population, as these are known to share bulk kinematic properties with the RC stars (Gaia Collaboration et al. 2021b).

During the course of our fitting, and as has been found in other work (e.g., Kallivayalil et al. 2013; Gaia Collaboration et al. 2021b), we found that the results for the LMC's kinematic center and bulk motion depend on the sample from which the fits derive. In particular, we found that fits to the younger red supergiants yielded a kinematic center that is consistent with the analysis from Gaia Collaboration et al. (2021, see their Table 5), allowed for the LMC's H I gas to trace the rotation

Table 1
The Best-fit Parameters to Describe the LMC Stellar Disk Kinematics

Parameter	Prior	Results
$v_{\rm sys}$ (km s^{-1}) (systemic velocity)	(250,275)	$264.046^{+0.375}_{-0.378}$
θ (deg) (line-of-node position angle)	(100,190)	$138.856^{+1.360}_{-1.370}$
i (deg) (inclination)	(15,45)	$23.396^{+0.493}_{-0.501}$
v_0 (km s^{-1}) (in-plane maximum rotation velocity)	(20,120)	$77.491^{+1.320}_{-1.247}$
η (scale radius/distance)	(0.02,0.2)	$0.067^{+0.001}_{-0.001}$
$\sigma_{v,\rm int}$ (km s^{-1}) (line-of-sight velocity dispersion)	(0,50)	$21.971^{+0.267}_{-0.261}$
$\sigma_{\mu_{\alpha*},\rm int}$ (mas yr^{-1}) (PM dispersion in α^*)	(0,2)	$0.124^{+0.002}_{-0.002}$
$\sigma_{\mu_{\delta},\rm int}$ (mas yr^{-1}) (PM dispersion in δ)	(0,2)	$0.138^{+0.002}_{-0.002}$
α_0 (deg) (LMC center in RA)	Fixed	80.443
δ_0 (deg) (LMC center in decl.)	Fixed	-69.272
$\mu_{\alpha*}$, 0 (mas yr^{-1}) (center-of-mass motion in α^*)	Fixed	1.859
μ_{δ}, 0 (mas yr^{-1}) (center-of-mass motion in δ)	Fixed	0.375

curve in a straightforward way, and yielded acceptable fits to the kinematics of the sample of older AGB and RGB stars. We thus fix the kinematic center and bulk PM to the values obtained for the red supergiant sample and fit the remaining parameters to the older RGB and AGB stars with radii <7°.5 from the LMC center. While a full discussion of the kinematic fits to different subsamples is beyond the scope of this paper, we note that our qualitative results do not depend on the precise center adopted. The full set of our fitting parameters, their priors, and the best fit for the RGB and AGB sample are summarized in Table 1, and the one-dimensional marginalized posterior probability distributions and two-dimensional joint posterior probability distributions for the fitting parameters are presented in Figure 2.

With the best-fit parameters in hand, we evaluate the key parameters used in the present study for our Gaia-selected RC stars based on their positions within the disk. The key parameters include the total model PM, the contribution of the LMC's center-of-mass motion to the total PM, and the contribution of internal rotation to the total PM. The inset in Figure 2 shows the comparison between the observed PMs and best-fit model-evaluated total PMs of the RC stars in the x- and y-directions, showing an excellent agreement between the observation and the best-fit kinematic model. This suggests that the observed stellar kinematics of the LMC is well described as an organized circular motion at the first order.

4. Results

4.1. Internal and Residual Proper Motions

Figure 3 shows the internal PM field (=observed PM field – the center-of-mass motion field) and the residual PM field (=observed PM field – total best-fit model PM field) in the left and middle panels, respectively. Here the total best-fit model
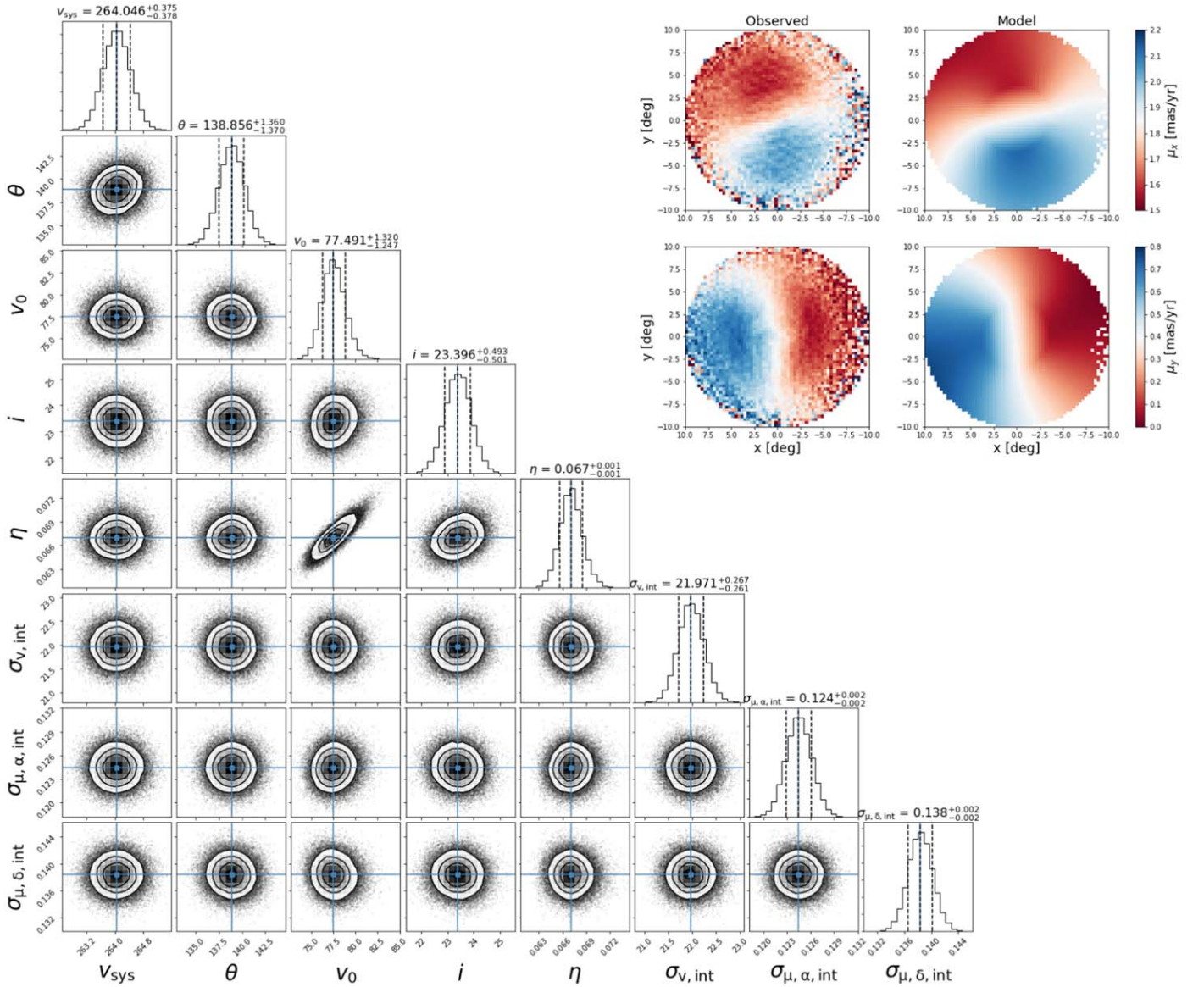
Figure 2. One-dimensional and two-dimensional posterior probability distribution functions of the fitting parameters for our best-fit kinematic model based on RGB and AGB stars that have both PM and line-of-velocity measurements. The inset in the upper right corner shows the observed PMs of the RC stars (left panels) and their best-fit model-evaluated PMs (right panels) in the x (top rows) and y (bottom rows) directions. The constructed PM field from the best-fit model well describes a disk rotation seen in the observed PM field.

PM field is the combination of the center-of-mass bulk motion and the internal rotation motion fields. On average, the LMC disk exhibits a well-organized clockwise (when seen by the observer) rotation, as shown in the literature.

Each vector field is constructed by taking mean motion in each $\sim0°\!.67$ by $\sim0°\!.67$ subregion, corresponding to ~580 pc at the LMC distance. The size of the subregion is chosen to secure sufficient signal-to-noise ratio (S/N) in the observed residual PM measurements for individual subregions; $\sim95\%$ of the subregions within $6°$ do have S/N > 3 (see below for the justification for the inner $6°$ analysis). The other factor we consider to choose the size of the subregion is the gravitational softening length of 100 pc in the simulations used in this study (see Section 5.1). Typically we do not trust much below 3–5 times the softening length because features on smaller physical scales are wiped out by numerical noise. Thus, this optimally chosen subregion size allows us to measure kinematic features from both the observation and the simulations with high

confidence. In addition, rigorous resolution tests show that our qualitative conclusions are robust against the choice of a subregion size from down to $3\times$ smaller to up to $4\times$ larger than the optimal subregion size.

Our best-fit kinematic model presented in Section 3 describes a rotation curve that linearly rises up to the maximum in-plane velocity of $77.491\,\mathrm{km\,s^{-1}}$ at 3.36 kpc from the center and then remains flat afterward, which is the typically expected pattern for a differentially rotating disk. However, the observed stars actually exhibit a declining rotation curve beyond $\sim6°$ (corresponding to ~5.25 kpc at the LMC distance) with different slopes for different position angles. The declining behavior of the stellar rotation velocity has been observed in the LMC before (e.g., Alves & Nelson 2000; van der Marel & Kallivayalil 2014; Wan et al. 2020; Gaia Collaboration et al. 2021b) and is partially attributed to elliptical orbits (van der Marel & Cioni 2001; see also Schmidt et al. 2022 for concurrent reporting of this result).
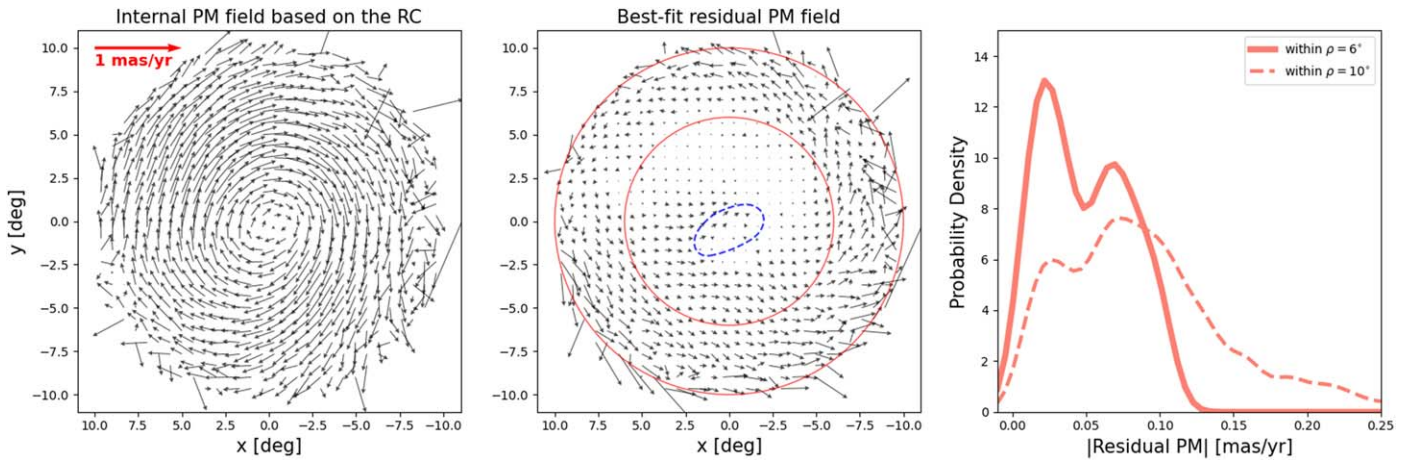
Figure 3. Observed internal motion field of the RC stars (left), residual PM field of the RC stars (middle), and distribution of the residual PM amplitudes of the RC stars within the inner 6° (right). We compute the internal motion of the RC stars by subtracting the center-of-mass motion contribution from the observed PM at each position in the LMC disk. The residual PM field of the RC stars is constructed by subtracting the best-fit model PM field, which includes both the center-of-mass motion and the internal rotation motion, from the observed PM field. To guide the eye, we place a 1 mas yr^{-1} scale bar in the left panel, galactic radius contours at 6° and 10°, and a rough outline of the observed bar (blue dashed line). The right panel shows the distributions of the residual PM amplitudes of the RC stars within the inner 6°, where we focus our comparison with the simulated galaxies in Section 5, and the inner 10°.

This position-angle-dependent declining rotation curve results in counterrotating motions with varying magnitude in the residual PM field at larger radius ($>6°$), where the observed rotation curve deviates from the best-fit kinematic model (middle panel of Figure 3). Therefore, we limit our analysis to the inner 6° in order to correctly evaluate the dynamical status of the LMC disk in a regime where our rotating disk model is valid.

In the inner 6°, the residual PM field shows clear asymmetric features; the residuals are larger in the southern disk than the northern disk, indicating that only the northern inner disk follows organized circular motions. The residual motions near the center might be due to highly noncircular motions around the tilted bar (e.g., Choi et al. 2018a). In the right panel of Figure 3, we present the Gaussian kernel density estimate (KDE) of amplitude distributions of the residual PMs measured using the RC stars within the inner 6° and 10°. The kinematic asymmetry is responsible for the bimodality of the distribution of the residual PM amplitudes (right panel of Figure 3). Larger residuals in the outer disk ($6° < \rho < 10°$) due to the declining rotation curve significantly contribute to the second peak and broaden the distribution for the inner 10°. The rms of the inner 6° distribution is 0.057 ± 0.002 mas yr^{-1} (see 0.056 mas yr^{-1} when taking the median, not mean, motion for the residual PM field construction). The standard error of the residual PMs' mean is ~ 0.003 mas yr^{-1} on average, and 95% of the subregions within 6° have S/N greater than 3 in the residual PM measurements. As presented in the Appendix, our RGB sample has the rms of ~ 0.058 mas yr^{-1} in the inner 6° distribution. This supports that the RC and RGB populations indeed share the statistically identical stellar kinematics despite their different brightness (i.e., completeness) and is consistent with the results shown by Gaia Collaboration et al. (2021b). In order to interpret and better understand these observed properties of the residual PM field, we compare the observation against baseline numerical models (see Section 5).

4.2. Connection between the Kinematic and Geometric Features in the LMC Disk

Before comparing the observed LMC with simulated LMC models, we first investigate the impact of a warped and twisted

disk on our default kinematic modeling, which assumes a single inclination and line-of-node position angles for the entire disk. As shown in the literature (e.g., van der Marel & Cioni 2001; Olsen & Salyk 2002; Choi et al. 2018a), the LMC disk is warped and twisted, likely due to the tidal interactions with the SMC. We repeat the kinematic fitting with the same set of RGB and AGB stars described in Section 3, but we only fit (i,θ) in each 1° width annulus, while fixing the rest of the parameters to be the best-fit parameters (Table 1). This allows us to see whether modeling the LMC disk as a twisted and warped disk could better reproduce the total observed PMs, leading to smaller residual PMs. In each 1° width annulus, we evaluate the model PMs based on the new best fit (i,θ), along with other parameters from the original best fit, and compute new residual PMs. The resulting composite residual PM field, however, still shows asymmetric features with a similar amplitude of the residual PMs. Although these new best-fit (i,θ) values for individual annuli are inevitably measured based on a smaller number of stars, no significant changes in the resulting residual PM field indicate that the twists and warps are not the main driver for the LMC's disk to deviate from simple circular motions. Nevertheless, this radially varying (i,θ) measurement enables us to explore potential connections between the kinematic and geometric features by making a direct comparison with the (i,θ) measurements made purely based on the three-dimensional geometry of the RC stars by Choi et al. (2018a). We note that this direct comparison is appropriate even though the completeness of the RC sample used in Choi et al. (2018a) and in the current study is different; the Survey of the MAgellanic Stellar History (SMASH) data have much higher RC completeness than the Gaia data (Nidever et al. 2017). This is because the stellar kinematics of the RC stars is independent of completeness as discussed in Section 2.

In Figure 4, we compare the kinematically and geometrically measured disk i and θ as a function of galactic radius. The radial trends found in the kinematically measured i and θ are broadly consistent with those found in the geometrically measured i and θ: decreasing i and θ with galactic radius with a significant turnover in i beyond 7°, where the southwest stellar
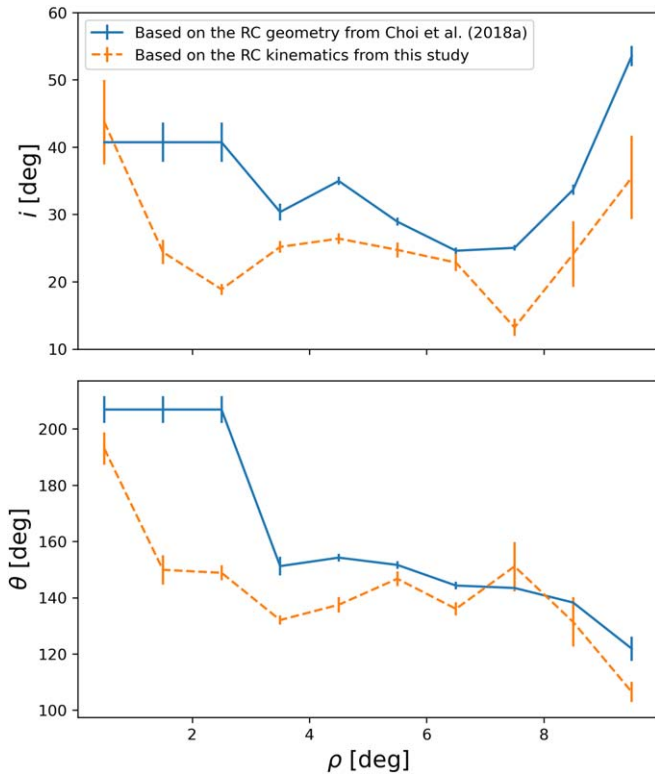
Figure 4. Comparison of the geometrically and kinematically measured i and θ in each 1° width annulus as a function of galactic radius. The geometrically measured i and θ values are from Choi et al. (2018a); they explored the three-dimensional geometry of the RC stars selected from the SMASH data (Nidever et al. 2017). We assumed that the measurements in the innermost two radial bins between 0° and 2°, where Choi et al. (2018a) did not make (i, θ) measurements, are the same as those made in the 2°–3° radial bin based on the consistency in those measurements between each annulus and each circle method as shown in their Figure 13.

warp is dominant. This suggests that the geometric distortions are imprinted in the stellar kinematics (or vice versa depending on which one happens first), and the LMC's disturbed stellar geometry and kinematics are the byproducts of a common event(s). Specifically, Choi et al. (2018a) attributed the radially varying i and θ within the LMC disk to the tilted bar and two stellar warps, likely induced by the recent direct collision with the SMC.

5. Comparison with Theoretical Models

5.1. Simulated LMCs from Besla et al. (2012)

Besla et al. (2012) presented numerical hydrodynamic simulations of the interacting LMC and SMC galaxies over the past 6–7 Gyr, including their entry into the Milky Way potential for the first time within the past 1 Gyr. Two models were explored, Model 1 and Model 2, with the primary difference between them being the interaction history of the LMC with the SMC. In Model 1, the SMC remains well separated from the LMC, with an impact parameter $\geqslant$20 kpc, over their entire interaction history (the LMC disk size is 18.5 kpc; see Nidever et al. 2019), including a duration of 5 Gyr prior to infall into the Milky Way halo. In Model 2, a recent direct collision (impact parameter $\sim$2 kpc) between the MCs occurs about 100 Myr ago, and the MCs have interacted for a duration of 6 Gyr prior to infall into the Milky Way halo. We note that, in Model 2, the most recent closest approach of

Table 2
Summary of the Six Simulated LMCs

Model Name	Impact Parameter (kpc)	Impact Timing (Myr ago)
Isolated	None	None
Model 1	20	100
Model 2	2	100
Future40	2	140
Future60	2	160
Future100	2	200

the SMC to the LMC (i.e., pericenter) coincides with the time when the SMC crosses the disk plane of the LMC (i.e., disk crossing), whereas, in Model 1, the disk crossing (pericenter) occurs $\sim$350 Myr (100 Myr) ago, when the separation between the MCs was $\sim$27 kpc (20 kpc, but 15 kpc below the LMC disk plane).

In each model the LMC's initial dark matter halo is modeled as a Hernquist profile with a total halo mass of $1.8 \times 10^{11} \, M_\odot$. The simulated stellar mass at the present day is $3.1 \times 10^9 \, M_\odot$, where the mass per stellar particle is 2500 $M_\odot$. The SMC is initially modeled as a Hernquist profile with a halo mass of $2.1 \times 10^{10} \, M_\odot$ before it begins interacting with the LMC on an eccentric, decaying orbit. Both models also account for the gravitational perturbations induced by a Milky Way halo mass of $10^{12} \, M_\odot$ as the MCs orbit over the past 1 Gyr. For details, please refer to Besla et al. (2012).

The authors argue that a direct collision is favored, as the structure and kinematics of the post-collision LMC and SMC simulations in Model 2 show better consistency with the observed properties of the MC system than in Model 1, at both large and small scales (e.g., Besla et al. 2016; Choi et al. 2018a, 2018b; Zivick et al. 2019). Given recent PM measurements for the SMC, it is highly improbable that the most recent encounter between the MCs occurred more than 300 Myr ago or at impact parameters larger than 20 kpc (Zivick et al. 2018). A collision scenario is thus unavoidable, but the exact timing and impact parameter of the encounter remains uncertain.

In this study we will examine in depth the stellar kinematics of the simulated LMC disk from the Besla 2012 models to gauge whether our study of the observed dynamical state of the real LMC can be used to inform us of the properties (timing, impact parameter) of the most recent LMC–SMC encounter.

To this end, we extract four additional LMC models from the same simulations by Besla et al. (2012). One model is for a completely undisturbed LMC disk ("Isolated"), and the other three models are 40, 60, and 100 Myr into the future since the Model 2 snapshot ("Future40," "Future60," "Future100"). These models correspond to 140, 160, and 200 Myr since the direct collision between the MCs. In total, we have six numerical models to compare against our Gaia data results: Isolated, Model 1 (impact parameter $\sim$20 kpc, 100 Myr ago), Model 2 (direct collision 100 Myr ago), Future40, Future60, and Future100. Table 2 summarizes the six simulated LMCs.

Each of these LMC models has >1 million star particles with full 6D position and velocity information in the Galactocentric coordinate system. The simulation also provides rough age estimates for stellar particles formed throughout the simulation. In this study we exclude star particles with ages younger than 1 Gyr old to focus on the intermediate to old stellar
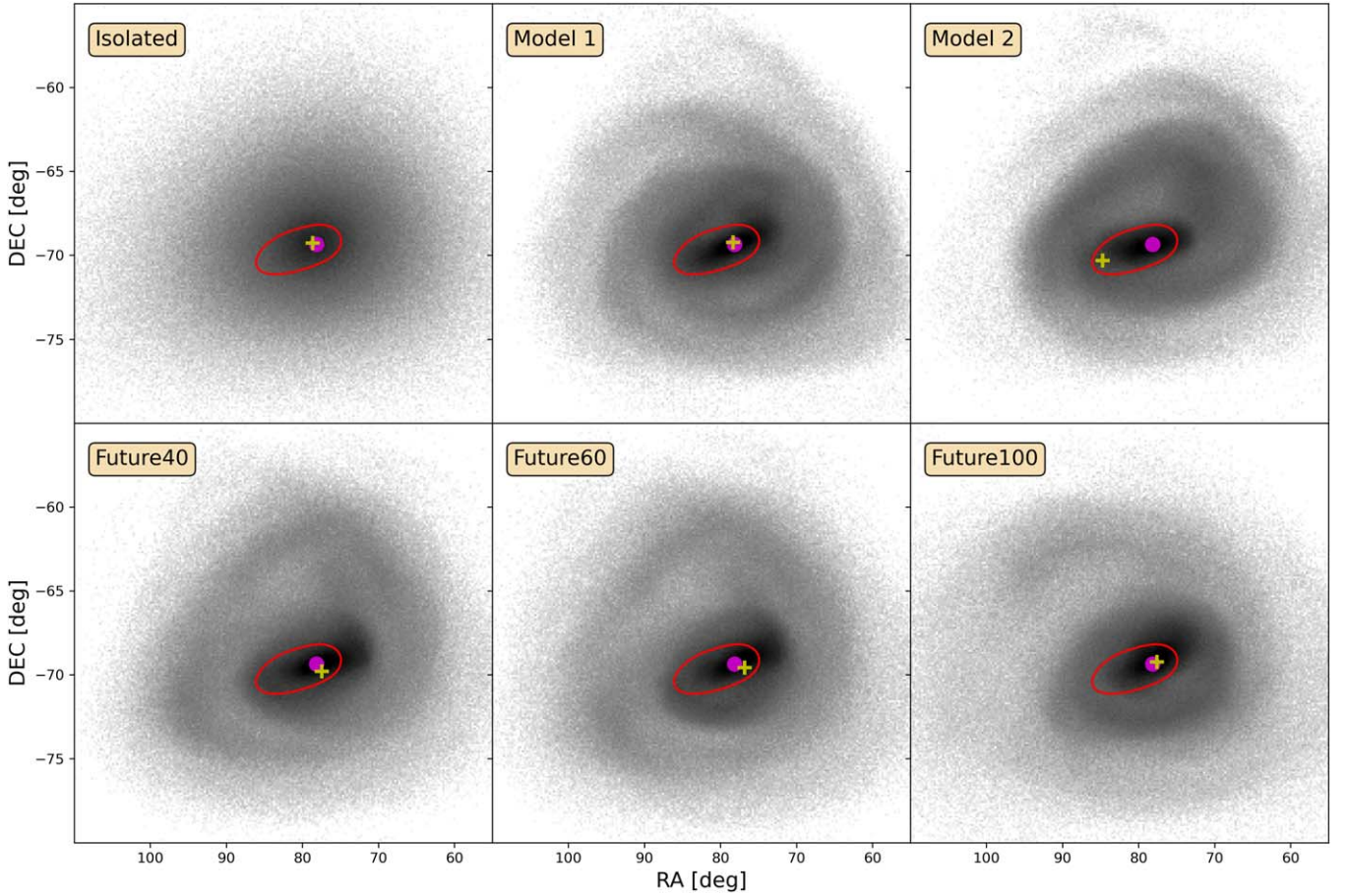
Figure 5. Star count maps using star particles formed >1 Gyr ago in the six numerical models considered in this study. In each simulation, the stellar mass per particle is 2500 $M_\odot$. From top left to bottom right: Isolated LMC, Model 1 (LMC with high impact parameter >20 kpc), Model 2 (direct collision ~100 Myr ago), Future40 (direct collision ~140 Myr ago), Future60 (direct collision ~160 Myr ago), and Future100 (direct collision ~200 Myr ago). Each modeled disk is also subject to the tidal field of a Milky Way host ($M_{\rm vir} = 10^{12}\,M_\odot$) as the LMC enters the Milky Way halo and orbits to its current location over the past 1 Gyr. We rotate each simulated LMC disk to a viewing perspective consistent with the real LMC disk and orientation of the bar. The rough location of the observed bar is outlined by the red ellipse. In each panel we mark the fixed center of mass of the simulated stellar disk with a magenta circle, while the kinematically derived center (see Section 3) is marked with a yellow plus sign.

populations, facilitating comparison with the observational results based on the RC stars.

To translate the simulations to the observed frame of reference of the LMC, we first recenter the center of mass and velocity of the simulated LMC stellar particles to be consistent with the Kallivayalil et al. (2013) values, $(X, Y, Z) = (-1, -41, -28)$ kpc and $(V_X, V_Y, V_Z) = (-57, -226, 221)$ km s^{-1}, and then rotate the model disks to match the observed viewing perspective ($i = 25°.86$, $\theta = 149°.23$; Choi et al. 2018a), corresponding to the normal vector of $(n_X, n_Y, n_Z) = (0.1332, 0.9628, 0.2348)$. Finally, we translate the positions and velocities of each star particle in the Galactocentric coordinate system into α and δ in the ICRS coordinate system, and $\mu_{\alpha*}$, μ_δ, and line-of-sight velocities using the `astropy.coordinates` package.

The resulting star count maps of the six model galaxies are projected on the sky and presented in Figure 5. For Models 1 and 2, we rotate the disks such that the simulated stellar bar is aligned with the observed bar in the LMC when projected on the sky. For Future40, Future60, and Future100, we correct the amount of rotation by accordingly counterrotating each disk to align the simulated stellar bar to the observed one, assuming a constant rotation velocity of 80 km s^{-1}, which is

consistent with the initial conditions for the simulations ("Isolated" LMC).

In each panel, the red ellipse roughly outlines the location of the observed LMC bar, and the magenta circle denotes the true center of mass of the simulated LMC, while the yellow plus sign marks the derived center of each simulated LMC from the star particles' kinematics (see Section 3). Even in the undisturbed case (Isolated), there is an offset of ($\Delta\alpha$, $\Delta\delta$) = ($-0°.483$, $-0°.081$) between the true center of mass and kinematically derived center. We confirm that this discrepancy originates from random sampling of star particles with number matched to our observed samples, hinting at the difficulty of defining the LMC center accurately with observational data. The rms values of offsets between the true center of mass of the simulated LMC and the kinematically derived center of each model are $2°.765$ and $0°.759$ in α and $0°.448$ and $0°.234$ in δ when including and excluding the most strongly perturbed LMC disk (Model 2), respectively. This clearly indicates that the strong direct collision with the SMC can significantly displace the kinematic center from the center of mass for a relatively short period of time since the impact (~100 Myr). The rms values of the offsets calculated including Model 2 are significantly larger compared to the range of
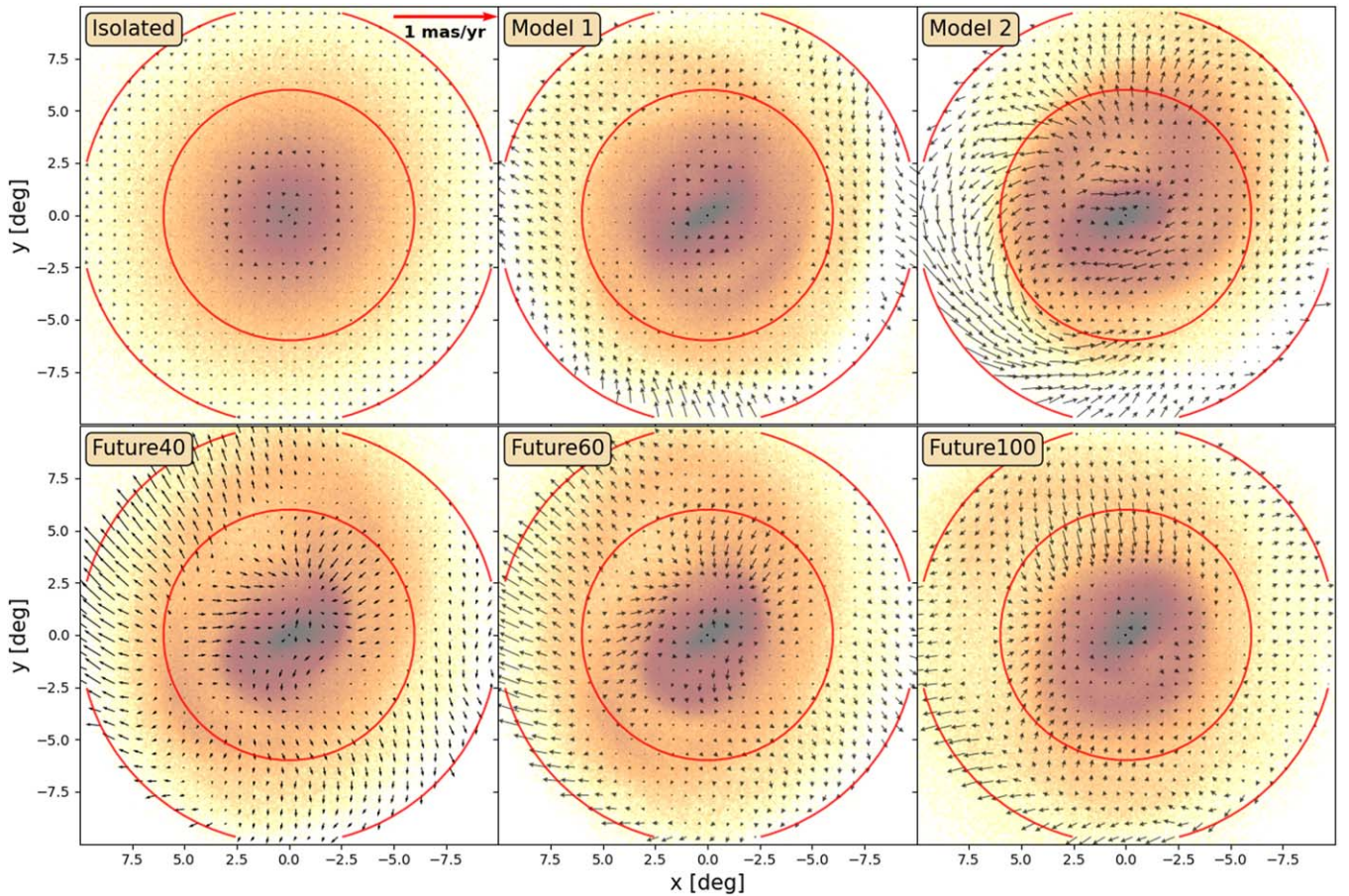
Figure 6. Residual PM fields for the six simulated LMCs: Isolated, Model 1, Model 2, Future40, Future60, and Future100, from top left to bottom right. The red circles denote the galactic radii of 6° and 10° to guide the eye. The blue dashed line marks the observed bar, as in Figure 3. The residual PM field of the Isolated model (i.e., unperturbed model) shows a low level of residuals in the inner ∼3° and in the outer ∼6°. These are the artifacts due to our assumed flat rotation curve in kinematic modeling. Thus, we subtract the Isolated model's residual PM field from the other five models to remove these artifacts.

reported kinematic centers for the observed LMC ($\sigma_\alpha = 1°.259$, $\sigma_\delta = 0°.359$; e.g., van der Marel & Kallivayalil 2014; Gaia Collaboration et al. 2021b). This analysis indicates that Model 2 (impact parameter <2 kpc within 100 Myr) results in an LMC disk with a kinematic center that strongly disagrees with observations. The results for Future40, Future60, and Future100 indicate that within an additional 40–100 Myr Model 2 does have sufficient time to settle to a dynamical state more consistent with observations. As such, a direct collision scenario is not ruled out, despite the large offsets exhibited in Model 2.

5.2. Residual Proper Motions of Simulated LMCs

For the six simulated galaxies that are translated to the observed frame (Section 5.1), we also conduct the kinematic modeling procedure to stellar particles that have six-dimensional phase-space information and derive the best-fit kinematic model for each simulated galaxy. We then evaluate the best-fit model-predicted PM components for individual star particles.

Figure 6 shows the residual PM fields for the six model galaxies. As described earlier, we compute observables (PMs on sky and line-of-sight velocity) for individual star particles in each simulated LMC. Using these simulated observables, we perform kinematic modeling for the six simulated LMCs and construct the residual PM fields based on the best-fit kinematic model for each simulated LMC. We fit all 12 parameters for

∼10,000 randomly selected star particles in each of the simulated LMCs.

The details of the PM residual fields for the simulated LMCs in Figure 6 depend on many details of the LMC–SMC interaction histories that are yet poorly constrained, e.g., the masses of the Milky Way, LMC, and SMC, the pre-collision structure of the galaxies, the pre-collision relative spin orientation of the galaxies, etc. Given the limited set of models assessed in this paper, it is therefore not surprising that the details of the observed residual field are not fully reproduced by any of the simulated LMCs. Instead, the amplitudes of the residuals are a direct measure of the disk heating induced by tidal interaction. This is less dependent on the details of the individual galaxies and is more directly driven by the impact parameter (smaller value yields more heating) and time that has passed since the collision, which enables post-collision cooldown. Since the impact parameter and timing are the orbital characteristics that we are most interested in here, we focus on a quantitative comparison of the amplitude distribution of the residuals and use the residual field itself only as an additional qualitative constraint (e.g., symmetric versus asymmetric).

The Isolated model shows tiny residual PMs (rms of 0.022 mas yr^{-1}) particularly in the central 3° and beyond 6° (top left in Figure 6). These features turn out to be the artifacts arising from a difference between the parameterized rotation curve assumed in the kinematic modeling and the resulting rotation curve from the mass profile for the initial, unperturbed

simulated LMC disk described in Section 5.1 (see also Besla et al. 2012). We therefore correct the residual PM fields of the other five simulated galaxies for the artifacts by subtracting the Isolated model's residual PM field and present the corrected fields in Figure 6. After making this correction, the Isolated model is no longer utilized.

To be consistent with the observational data, we limit our analysis of the five simulated galaxies to the inner 6° as well. This also minimizes the potential bias in the residual PM fields due to uncertainties in the importance of the Milky Way tidal field (i.e., the uncertainties in the mass of the Galaxy), which will largely impact the outskirts of the LMC disk. In addition, the future models (Future40, Future60, and Future100) interact with the Milky Way for a longer period of time than Models 1 and 2, leading to inconsistent Milky Way tidal fields in the outer disk.

Nonuniform residual PM features in the inner 6° are found in all five simulated LMCs, which is consistent with the observational data (see Figure 3). However, the strength of the residuals varies across the models. Model 1 (LMC–SMC impact parameter ∼20 kpc about 100 Myr ago) is left with insignificant residuals, making it consistent with a marginally perturbed disk. On the other hand, the other simulated galaxies maintain more prominent residuals and asymmetric kinematic features in the inner 6°. Specifically, Model 2 (direct collision with an impact parameter of 2 kpc about 100 Myr ago) shows net streaming motions from west to east and from east to west under and above the bar, respectively, and then diverging motion to the north and east. The Future40, Future60, and Future100 models, roughly speaking, present a net inward motion toward the central disk in the inner 3°–6°, which is not clear in the data (see Figure 3).

In Figure 7, we compare the KDEs of the residual PM amplitudes for the observed RC stars and the five simulated LMCs within the inner 6°, where there are no complexities associated with rotation curve modeling, making our comparison straightforward. The top panel compares the observation with the results from Models 1 and 2, while the bottom panel compares with Model 2 and its future snapshots (Future40, Future60, and Future100). The rms values of each model's residual PM distributions are 0.027, 0.084, 0.062, 0.062, and 0.067 mas yr^{-1} for Model 1, Model 2, Future40, Future60, and Future100, respectively.

The distribution of the residual PM amplitudes of Model 1 is completely inconsistent with the observation in terms of its morphology and rms. Model 1 seems to be perturbed much less compared to the observed LMC disk; it has significantly smaller rms and no evidence for kinematic asymmetry (i.e., well described as a single Gaussian). On the other hand, Model 2 shows a clear evidence of multiple peaks, a sign of kinematic asymmetry, as seen in the observed data. Nevertheless, Model 2 is dynamically too hot (significantly larger rms) to explain the observed LMC's disk, suggesting that more time is required for Model 2 to dynamically cool down to be consistent with the observation. Thus, the dynamical status of the present-day LMC likely lies between Models 1 and 2.

In the bottom panel of Figure 7, we compare the observations and the results from Model 2 (100 Myr after the collision) and its future snapshots, Future40 (140 Myr after the collision), Future60 (160 Myr after the collision), and Future100 (200 Myr after the collision), to more closely investigate the time evolution of the LMC stellar kinematics after a direct collision with the SMC. The
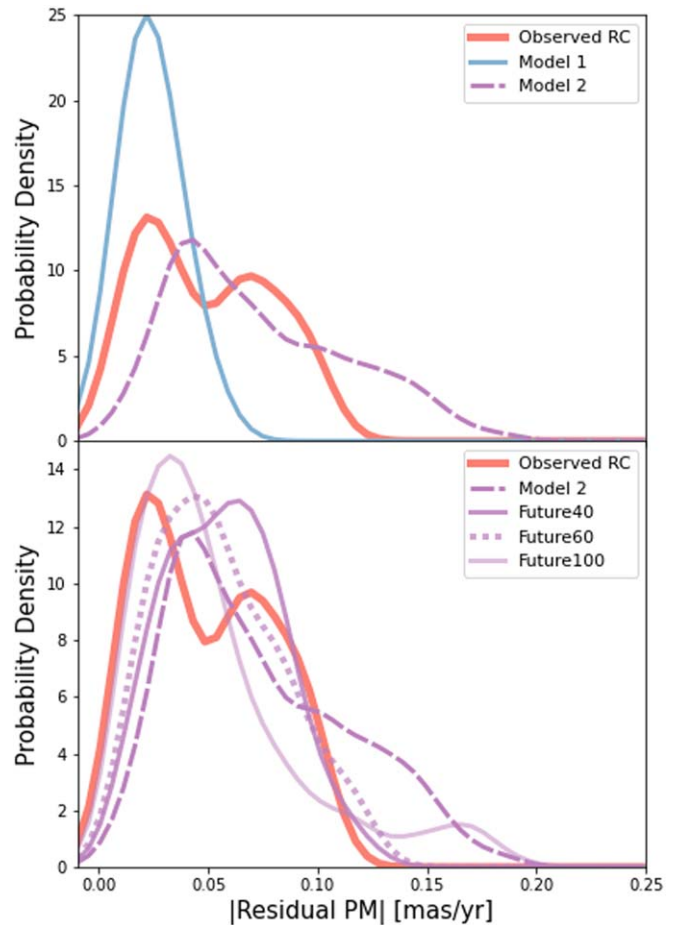

Figure 7. Gaussian KDEs showing distributions of the residual PM amplitudes within the inner 6° for the observed RC and RGB stars, along with those for the five simulated LMC galaxies that are calibrated using the Isolated model residual PM field.

residual PM amplitudes rapidly decrease from Model 2 to its future snapshots. The perturbation in Model 2 is significantly damped by ∼25% during the first 40 Myr and then remains more or less the same for the next 60 Myr with a slight increase in Future100. In terms of rms values, all future models are consistent with each other and more perturbed than Model 1. In addition, they show a hint of kinematic asymmetry via a few bumps or broadening in their distributions, which is consistent with the observation. However, contrary to Future40 and Future60, as well as the observation, Future100 shows a significantly extended tail toward higher residuals as much as Model 2, but with significantly lower probability density, which makes its rms value increase compared to Future40 and Future60 despite its narrower distribution in the smaller residual regime. On average, the dynamical status of the three future models is consistent with that observed, suggesting that the present-day LMC should have evolved for at least 140 Myr since the last collision if the collision was direct with an impact parameter of 2 kpc. Utilizing the smallest probable impact parameter from the LMC–SMC analytic orbit modeling of ∼2 kpc (Zivick et al. 2018), this required time of 140 Myr sets the lower limit to the timing of such a collision.

5.3. Constraining the Recent Collision with the SMC

A clear trend from the residual PM amplitudes of the five simulated LMCs is that the degree of perturbation decreases

with either longer impact timing T (i.e., longer elapsed time since the last encounter between the MCs) or larger impact parameter P (i.e., larger separation between the LMC and SMC at the time of impact). For example, an LMC disk with a direct collision with a more modest impact parameter (e.g., 10 kpc) than Model 2 would have had less disk heating initially and hence would have needed less time to cool down to reproduce the observed amplitude residuals than Model 2. To analytically describe this trend, we fit a simple planar model to log of the rms (mas yr^{-1}) of the residual PM amplitude distribution as a function of impact timing in Myr and impact parameter in kpc, which yields the correct asymptotic behavior toward longer impact timing and larger impact parameter. The best-fit plane based on the five simulated LMCs is

$$\log_{10}(\mathrm{rms}) = -0.000946\,T - 0.0274\,P - 0.974. \qquad (1)$$

The top panel of Figure 8 shows the predicted rms values in log scale as a function of (T, P). We depict the possible one-dimensional family of (T, P) that is consistent with the observations. With the caveat that this plane fitting is based on very limited parameter space and thus should be considered as the first-order approximation, we find that the observations disfavor a distant encounter scenario with an impact parameter >20 kpc but favor a close impact scenario with an impact parameter <10 kpc. Furthermore, we find that perturbations induced by an SMC collision ~ 250 Myr ago (with any impact parameter larger than 2 kpc) will always be weaker than that observed. This is consistent with the upper limit placed on the impact timing and impact parameter for the LMC–SMC collision inferred from orbit modeling using the observed PMs of the MCs (Zivick et al. 2018). We also find that, for a no direct collision case like Model 1 (i.e., impact parameter $>$LMC disk), the observed level of disk heating cannot be reproduced even if we observed the LMC right after the encounter, which is inconsistent with the observed relative separation (~ 20 kpc) and velocity (~ 100 km s^{-1}) between the LMC and SMC (Zivick et al. 2018). The minimum probable T from orbit modeling is ~ 80 Myr (Zivick et al. 2018, their Figure 12). Combining this with our results places an upper limit on the impact parameter of ~ 7.5 kpc.

The edge-on view of the best-fit plane is also presented in the bottom panel of Figure 8, along with the positions of the five simulated LMCs and the observation. If we take this simple best-fit plane at face value, the observation best agrees with Future100. However, given our small sample of simulated LMCs with very limited coverage of the parameter space, there is insufficient evidence to exclude Future40 and Future60. Furthermore, all the Future models reside close to each other in the $(T, P, \log_{10}(\mathrm{rms}))$ space. However, we can rule out Models 1 and 2. This analysis places a lower limit on the timing of the collision, given an impact parameter. In particular, if the collision was direct (<5 kpc; Model 2, Future40, Future60, Future100), then the collision cannot have occurred within $\leqslant 150$ Myr. Based on LMC–SMC orbit modeling, the most probable impact timing is 147 ± 33 Myr ago (Zivick et al. 2018, their Figure 12). From our plane fitting, this would suggest that the collision would have occurred with the impact parameter of $5^{+1.5}_{-1}$ kpc. This impact parameter, inferred based on the PM residuals, is also consistent with the expected impact position of the collision from orbit modeling (7.5 ± 2.5 kpc) within uncertainty.

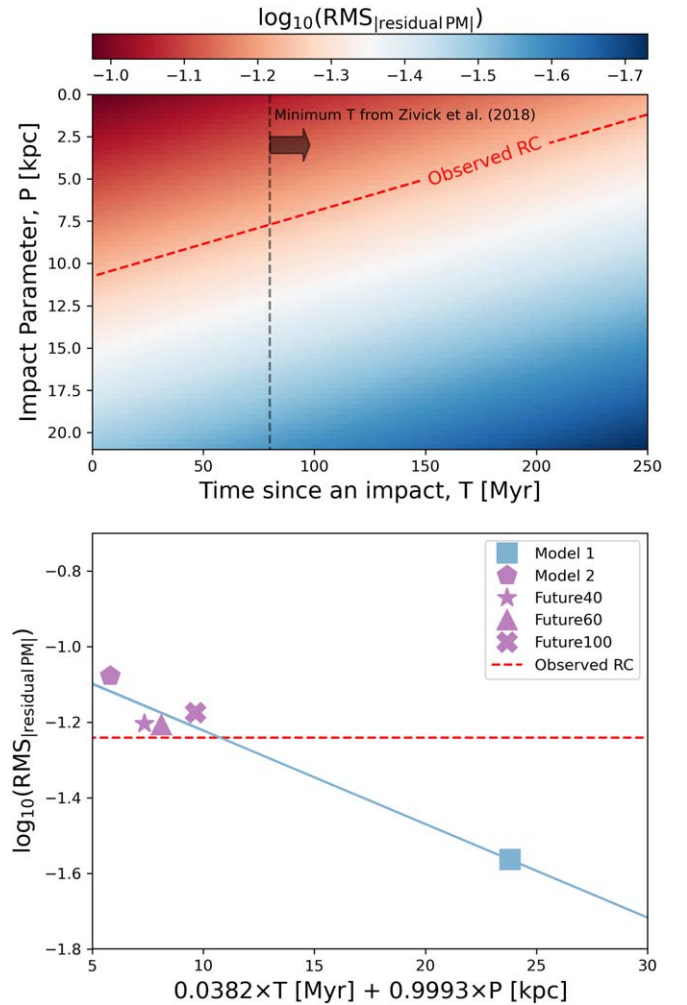While Models 1 and 2 are isolated in this space, the observation is clustered around Future40, Future60, and

Figure 8. Top: predicted log10 of an rms of a residual PM amplitude distribution as a function of impact timing (T) and impact parameter (P). The prediction is made from the best-fit plane of (T, P, log10(rms)) using the five simulated LMCs. The red dashed line indicates the one-dimensional family of (T, P) that is consistent with the RC-based observational results. The black dashed line denotes the minimum T from the LMC–SMC orbit modeling (Zivick et al. 2018). Bottom: the edge-on view of the best-fit plane (blue solid line) and distribution of the five simulated LMCs around the plane. The observation agrees reasonably well with all three future models (Future40, Future60, and Future100).

Future100. As expected from its KDE presented in Figure 7, no significant asymmetric feature in the residual PM field is found in Model 1, indicating that a direct collision is necessary to develop the asymmetric features in the stellar kinematics measured in the observational data. Together with the rms values, the asymmetry further supports that the dynamical states of the Future models are similar and consistent with the observed LMC stellar disk. In conclusion, the present-day dynamical status of the LMC disk requires that the most recent encounter with the SMC be direct, with an impact parameter $\leqslant \sim 10$ kpc and impact timing of <250 Myr, based on our analysis *alone*. If we adopt the impact timing constraint of ~ 140–160 Myr ago from analytic orbit modeling of the LMC–SMC (Zivick et al. 2018) and from the star formation history in the Magellanic Bridge (e.g., Harris 2007; Noël et al. 2015), then the impact parameter must be ~ 5 kpc. This necessarily means that the recent close encounter also coincides with the time when the SMC crosses the LMC disk plane.

Note that the orbit modeling presented in studies like Zivick et al. (2018) consists of analytic calculations that do not account for the distortions to the dark matter halos of the MCs during their interaction; this will influence the true range of plausible impact parameters and timing of the collision. As we have illustrated through comparison to the Besla et al. (2012) models, the PM residuals presented in this paper provide a novel way to validate the assumed impact parameter and timing of the LMC–SMC collision when combined with numerical modeling.

6. Summary and Conclusion

We explore the kinematics of the RC stars of the LMC selected from the Gaia EDR3 catalog. Using the kinematic model best describing the three-dimensional motion of old stellar populations, we construct the residual PM field for the RC stars by subtracting the center-of-mass motion field and the internal rotation motion field from the observed PM field. We focus on the residual PM field in the inner $6°$, where our rotation curve modeling is valid and there are minimal perturbations from Milky Way tides. We also derive the disk inclination and the line-of-node position angles as a function of galactic radius based on stellar kinematics in each $1°$ width annulus, and we compare the results to those based on the three-dimensional geometry of the RC stars. Our main findings from the kinematic analysis of the RC stars in the LMC are as follows:

1. The resulting residual PM field reveals asymmetric patterns, including a complex residual PM field around the bar, larger residual PMs in the southern disk than the northern disk, and counterrotating residual motion with varying amplitude as a function of position angle.
2. The rms of the residual PM amplitude distribution, a proxy for disk heating, is $0.057 \pm 0.002\,\mathrm{mas\,yr^{-1}}$.
3. The radial trends of kinematically and geometrically derived inclination and line-of-node position angles are consistent with each other, indicating that the perturbed kinematics and distorted geometry likely have the same origin. In particular, a rapid increase in the geometrically derived inclination beyond $\sim7°$ is attributed to the outer stellar warp in the southwest part of the LMC disk, a likely byproduct of the recent direct collision with the SMC (Choi et al. 2018a). The same behavior in the kinematically derived inclination suggests that the tidal event that induced the stellar warp has also been imprinted in the stellar kinematics.

To assess the dynamical state of the present-day LMC disk, we compare the observed stellar kinematics to five numerical simulations of an LMC with different interaction histories with the SMC in a first infall scenario (Besla et al. 2012). Following the same methodology applied to the observational data, we obtain the residual PM fields and measure the rms of the residual amplitude distribution for five simulated LMCs. We find that the level of disk heating and asymmetric feature of the residual PM field of the present-day LMC disk are consistent with those exhibited by the Future models (Future40, Future60, Future100) in which an LMC underwent a direct collision with the SMC with an impact parameter of 2 kpc 140–200 Myr ago. Although an asymmetric feature exists in Model 2 (only 100 Myr after the direct collision with the SMC), its disk is dynamically too hot (rms of $0.084\,\mathrm{mas\,yr^{-1}}$) to explain the observational results. On the other hand, Model 1, where the impact parameter between the MCs remains larger than the radius of the LMC's stellar disk, is inconsistent with the observational results in both disk heating and kinematic asymmetry; the rms of the residual PM amplitudes is too small $(0.027\,\mathrm{mas\,yr^{-1}})$, and asymmetry is not clearly seen in the residual PM field. Similarly, the PM residual for an isolated, unperturbed LMC disk is also inconsistent with the data, indicating that the present-day LMC disk is not in dynamical equilibrium.

Our comparisons of the observed and simulated LMCs suggest the following:

1. A direct collision (i.e., impact parameter <LMC disk size) is needed to simultaneously reproduce the observed level of disk heating and asymmetry in the stellar kinematics. Thus, Model 1 (large impact parameter 20 kpc about 100 Myr ago) can be safely excluded. This further indicates that the tidal field of the Milky Way alone is insufficient to reproduce the asymmetry and level of disk heating observed in the LMC disk; a direct collision with the SMC is required.
2. For an LMC with a strong direct SMC collision (impact parameter of 2 kpc), the impact must have occurred at least 140 Myr ago in order for the LMC disk to have sufficient time to dynamically cool down and reach a similar dynamical state to that observed in the present-day LMC. Thus, Model 2 (only 100 Myr since the collision) can also be safely excluded. This timing for a direct collision is consistent with independent constraints from the LMC–SMC orbital modeling (Zivick et al. 2018) and with the ages of young stars in the Magellanic Bridge (Harris 2007; Noël et al. 2015).
3. Perturbations induced by a direct collision (with any impact parameter <10 kpc) will be significantly damped after 250 Myr and become unable to reproduce the present-day LMC's level of disk heating. This sets a stringent upper limit on the timing of a direct collision between the MCs based on dynamics.
4. Based on our PM residual analysis, we conclude that the most recent encounter with the SMC is direct, with an impact parameter $\lesssim10$ kpc and timing within the past 250 Myr. If we adopt the timing constraints from the analytic orbit modeling of Zivick et al. (2018) and the star formation history in the Magellanic Bridge (e.g., Harris 2007; Noël et al. 2015), our combined results suggest that the recent collision occurred ~140–160 Myr ago with an impact parameter of ~5 kpc, meaning that the recent close encounter also inevitably coincides with the time when the SMC crosses the LMC disk plane.

Given that analytic orbital modeling methods cannot account for the distortions to the dark matter halos of the LMC or SMC, we advocate that the PM residuals presented in this paper are a novel and important constraint that should be used to assess the validity of numerical simulations with a given impact parameter and timing of the LMC–SMC collision.

Appendix

To ensure that our results are indeed independent of tracers among old stellar populations, we also perform the same analyses using the RGB stars, which are brighter than the RC stars and thus have smaller Gaia PM measurement errors and higher completeness (Gaia Collaboration et al. 2021b). We select the RGB stars using the same spatial and Gaia cuts to the RC stars, but with a different CMD selection. The RGB selection polygon in the CMD is defined as follows: (BP−RP, G) = ((1.4, 18.3), (1.8, 16.5), (2.1, 15.9), (1.8, 15.75), (1.5, 16.5), (1.18, 18.0), (1.4, 18.3)). Figure A1 describes our RGB sample selection. This

selection criteria successfully exclude stars with ruwe > 1.23 and astrometric_excess_noise_sig > 2, resulting in a total of 488,795 RGB stars in our final sample. Despite the smaller sample size compared to the RC sample, the fraction of pixels within 6° with residual PM S/N < 3 is only ∼2%.

In Figure A2, we present the internal motion and residual PM fields of the RGB sample in the left and middle panels, respectively. The RGB internal motion field also shows a well-organized disk rotation as seen in the RC sample (see Figure 3). The residual PM field shows the same general behaviors as the RC sample—larger residuals beyond 6° due to the declining rotation curve and asymmetric features. Within the inner 6°, one noticeable difference between the RC and RGB samples is that the kinematic asymmetric features appear in different parts of the disk. While the RC residual PM field shows a rough north–south dichotomy, the RGB one is more stochastic with a couple of lower residual spots in the east and west sides of the disk and southeast of the bar, leading to a much smoother distribution of the residual PM amplitude than that of the RC sample, i.e., no bimodality. To understand the origin of the spatial discrepancy in the residual PM fields between the RC and RGB populations, a more complex analysis might be required, which is beyond the scope of this paper. Nevertheless, the rms of the distribution for the RGB sample is $0.058 \pm 0.002 \, \mathrm{mas \, yr^{-1}}$, suggesting the same level of the disk
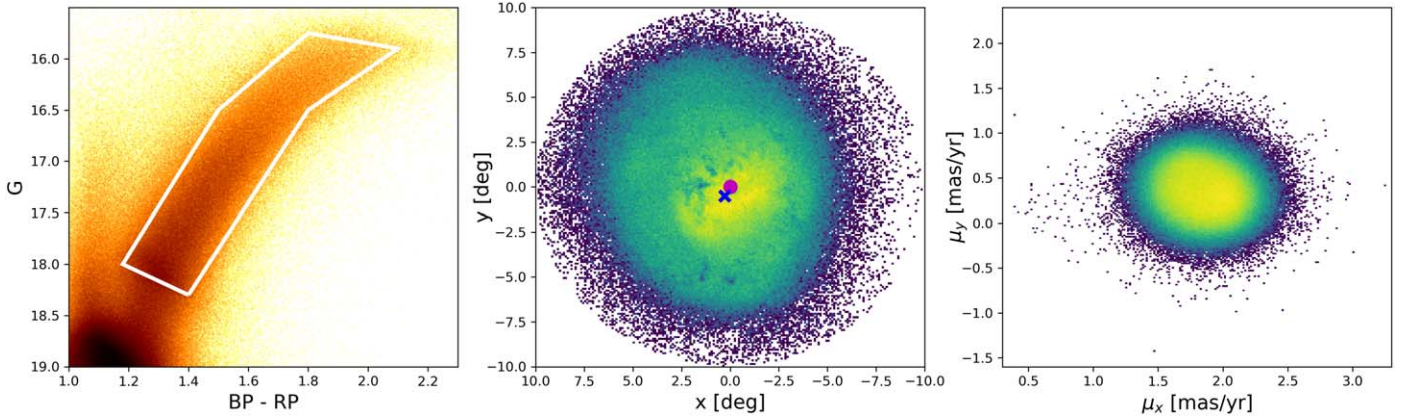

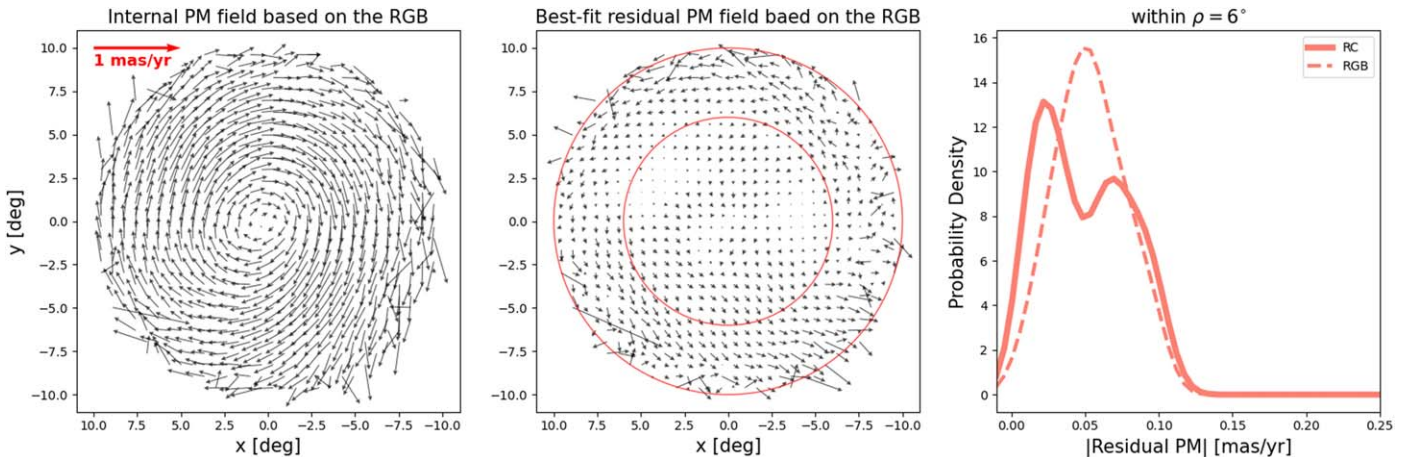**Figure A1.** Same as Figure 1, but for the RGB selection.

Figure A2. Same as Figure 3, but for the RGB sample. The first two panels show the internal motion field and residual PM field of the RGB stars. In the third panel, we compare the distribution of the residual PM amplitudes of the RC (solid curve) and RGB (dashed curve) stars within the inner 6°.

heating as we measure with the RC sample. Due to this consistent rms value, our constraints on the impact timing and parameter remain the same for the RGB sample.

In summary, our main conclusions do not depend on the choice of tracers between the RC and RGB populations. This is consistent with the study by Gaia Collaboration et al. (2021b), where they showed that their RC and RGB subsamples from Gaia EDR3 share very similar stellar kinematics.

ORCID iDs

Yumi Choi ● https://orcid.org/0000-0003-1680-1884
Knut A. G. Olsen ● https://orcid.org/0000-0002-7134-8296
Gurtina Besla ● https://orcid.org/0000-0003-0715-2173
Roeland P. van der Marel ● https://orcid.org/0000-0001-7827-7825
Paul Zivick ● https://orcid.org/0000-0001-9409-3911
Nitya Kallivayalil ● https://orcid.org/0000-0002-3204-1742
David L. Nidever ● https://orcid.org/0000-0002-1793-3689

References

Ahumada, R., Prieto, C. A., Almeida, A., et al. 2020, ApJS, 249, 3
Alves, D. R., & Nelson, C. A. 2000, ApJ, 542, 789
Astropy Collaboration, Robitaille, T. P., Tollerud, E. J., et al. 2013, A&A, 558, A33
Besla, G., Hernquist, L., & Loeb, A. 2013, MNRAS, 428, 2342
Besla, G., Kallivayalil, N., Hernquist, L., et al. 2007, ApJ, 668, 949
Besla, G., Kallivayalil, N., Hernquist, L., et al. 2012, MNRAS, 421, 2109
Besla, G., Martínez-Delgado, D., van der Marel, R. P., et al. 2016, ApJ, 825, 20
Boubert, D., & Everall, A. 2020, MNRAS, 497, 4246
Choi, Y., Nidever, D. L., Olsen, K., et al. 2018a, ApJ, 866, 90
Choi, Y., Nidever, D. L., Olsen, K., et al. 2018b, ApJ, 869, 125
Cioni, M. R. L., Clementini, G., Girardi, L., et al. 2011, A&A, 527, A116
Foreman-Mackey, D., Hogg, D. W., Lang, D., & Goodman, J. 2013, PASP, 125, 306
Foreman-Mackey, D., Farr, W., Sinha, M., et al. 2019, JOSS, 4, 1864
Freedman, W. L., Madore, B. F., Gibson, B. K., et al. 2001, ApJ, 553, 47
Gaia Collaboration, Brown, A. G. A., Vallenari, A., et al. 2021a, A&A, 649, A1
Gaia Collaboration, Luri, X., Chemin, L., et al. 2021b, A&A, 649, A7
Girardi, L. 2016, ARA&A, 54, 95
Girardi, L., & Salaris, M. 2001, MNRAS, 323, 109
Górski, M., Zgirski, B., Pietrzyński, G., et al. 2020, ApJ, 889, 179
Harris, J. 2007, ApJ, 658, 345
Haschke, R., Grebel, E. K., & Duffau, S. 2011, AJ, 141, 158
Hunter, J. D. 2007, CSE, 9, 90
Kallivayalil, N., van der Marel, R. P., Alcock, C., et al. 2006, ApJ, 638, 772
Kallivayalil, N., van der Marel, R. P., Besla, G., Anderson, J., & Alcock, C. 2013, ApJ, 764, 161
Lindegren, L., Klioner, S. A., Hernández, J., et al. 2021, A&A, 649, A2
Murray, C. E., Peek, J. E. G., Di Teodoro, E. M., et al. 2019, ApJ, 887, 267
Newville, M., Otten, R., Nelson, A., et al. 2021, lmfit/lmfit-py 1.0.2, 1.0.2, Zenodo, doi: 10.5281/zenodo.4516651
Nidever, D. L., Olsen, K., Choi, Y., et al. 2019, ApJ, 874, 118
Nidever, D. L., Olsen, K., Walker, A. R., et al. 2017, AJ, 154, 199
Noël, N. E. D., Conn, B. C., Read, J. I., et al. 2015, MNRAS, 452, 4222
Oey, M. S., Dorigo Jones, J., Castro, N., et al. 2018, ApJL, 867, L8
Olsen, K. A. G., & Salyk, C. 2002, AJ, 124, 2045
Olsen, K. A. G., Zaritsky, D., Blum, R. D., Boyer, M. L., & Gordon, K. D. 2011, ApJ, 737, 29
Pardy, S. A., D'Onghia, E., Athanassoula, E., Wilcots, E. M., & Sheth, K. 2016, ApJ, 827, 149
Riello, M., De Angeli, F., Evans, D. W., et al. 2021, A&A, 649, A3
Schmidt, T., Cioni, M.-R. L., Niederhofer, F., et al. 2020, A&A, 641, A134
Schmidt, T., Cioni, M.-R. L., & Niederhofer, F. 2022, arXiv:2201.10018
Skowron, D. M., Skowron, J., Udalski, A., et al. 2021, ApJS, 252, 23
Subramaniam, A., & Subramanian, S. 2009a, ApJL, 703, L37
Subramanian, S., & Subramaniam, A. 2009b, A&A, 496, 399
Subramanian, S., & Subramaniam, A. 2013, A&A, 552, A144
Udalski, A., Szymański, M. K., & Szymański, G. 2015, AcA, 65, 1
van der Marel, R. P. 2001, AJ, 122, 1827
van der Marel, R. P., Alves, D. R., Hardy, E., & Suntzeff, N. B. 2002, AJ, 124, 2639
van der Marel, R. P., & Cioni, M.-R. L. 2001, AJ, 122, 1807
van der Marel, R. P., & Kallivayalil, N. 2014, ApJ, 781, 121
van der Marel, R. P., & Sahlmann, J. 2016, ApJL, 832, L23
van der Walt, S., Colbert, S. C., & Varoquaux, G. 2011, CSE, 13, 22
Virtanen, P., Gommers, R., & Oliphant, T. E. 2020, NatMe, 17, 261
Wan, Z., Guglielmo, M., Lewis, G. F., Mackey, D., & Ibata, R. A. 2020, MNRAS, 492, 782
Yoshizawa, A. M., & Noguchi, M. 2003, MNRAS, 339, 1135
Yozin, C., & Bekki, K. 2014, MNRAS, 439, 1948
Zaritsky, D. 2004, ApJL, 614, L37
Zhao, H., & Evans, N. W. 2000, ApJL, 545, L35
Zivick, P., Kallivayalil, N., Besla, G., et al. 2019, ApJ, 874, 78
Zivick, P., Kallivayalil, N., van der Marel, R. P., et al. 2018, ApJ, 864, 55